



Photocatalytic activity of TiO₂ polycrystalline sub-micron fibers with variable rutile fraction



Jian Liu^a, Danielle L. McCarthy^a, Michael J. Cowan^a, Emily A. Obuya^b, Jared B. DeCoste^{c,d}, Kenneth H. Skorenko^a, Linyue Tong^a, Steven M. Boyer^a, William E. Bernier^a, Wayne E. Jones Jr.^{a,*}

^a Department of Chemistry, Binghamton University–State University of New York, Binghamton, NY 13902, USA

^b Department of Chemistry and Biochemistry, Russell Sage College, 65 First Street, Troy, NY 12180, USA

^c Leidos, Inc., P.O. Box 68, Gunpowder, MD 21010, USA

^d Edgewood Chemical Biological Center, 5183 Blackhawk Road, Aberdeen Proving Ground, MD 21010, USA

ARTICLE INFO

Article history:

Received 28 July 2015

Received in revised form

17 December 2015

Accepted 22 December 2015

Available online 15 January 2016

Keywords:

Photocatalyst

Rutile fraction

Grain size

Electron–hole separation

Pharmaceutical agents

ABSTRACT

TiO₂ polycrystalline sub-micron fibers can be used as photocatalysts for the degradation of a variety of organic molecules. Here we report on the optimization of these fibers for decontaminating pharmaceutical agents in aqueous medical waste streams. Mixed-phase TiO₂ fibers have been prepared via a sol–gel technique followed by electrospinning and calcination. By adjusting the calcination temperature, the rutile phase fraction in TiO₂ fibers can be tuned relative to the anatase phase from 0% to 100%. The effect of rutile phase fraction on grain size and specific surface area as well as their subsequent influences on the photocatalytic activity was investigated. An optimal grain size in post-calcined TiO₂ fibers was found to be critical to balance the e[−]/h⁺ volume recombination, surface recombination rate, and charge diffusion rate. The photocatalytic activities of the post-calcined TiO₂ fibers with different rutile fractions were measured by monitoring the decreasing concentration of phenazopyridine in aqueous solution under UV illumination using UV–vis absorption spectroscopy. Post-calcined TiO₂ fibers composing of 38 wt% rutile and 62 wt% anatase exhibited the highest initial degradation rate constant of 0.044 min^{−1}. This optimal photocatalytic activity can be attributed to the combined influences of the fibers' phase composition, surface area and grain size.

© 2016 Elsevier B.V. All rights reserved.

1. Introduction

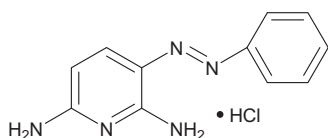
Many pharmaceutical and medical facility waste streams are considered hazardous and toxic. Hospitals, nursing homes, private clinics, and laboratories are a growing source of this type of environmental pollution [1,2]. Residual and waste drugs are discarded into environmental waters through sewers with human waste or direct disposal causing serious contamination. A number of conventional techniques, such as dilution and incineration [3], are widely used to minimize the impact, however they still cannot be removed from contaminated water efficiently. Advances in the field of chemistry have resulted in many improved methods for environmental cleanup. One main focus of study has been using photocatalysts to degrade environmental pollutants [4–8].

Fujishima and Honda first reported that TiO₂ exhibited a photocatalytic activity [9]. Since the initial discovery, it has been regarded as an efficient photocatalyst for degradation of organic pollutants from water due to its strong oxidative power, high stability, low cost and environmental friendliness [10–16]. The three polymorphs of TiO₂, anatase, rutile and brookite, show very different photocatalytic activities. The photocatalytic activity of TiO₂ is related to several different factors including electronic structure, degree of crystallinity, specific surface area, porosity, and crystal size [17–21]. Compared to the pure rutile phase, the anatase phase of TiO₂ exhibits better photocatalytic activity due to its higher adsorption affinity for organic molecules [22] and lower electron–hole recombination rate [23–26].

Meanwhile, it has been known that anatase nanopowders with a small fraction of rutile phase, such as commercial TiO₂ Degussa P25 consisting of ~20 wt% rutile and ~80 wt% anatase, show an enhanced photocatalytic activity compared with pure anatase powders due to enhanced electron and hole transfer between the two phases [24,27]. The synergistic effect between TiO₂ anatase and

* Corresponding author.

E-mail address: wjones@binghamton.edu (W.E. Jones Jr.).



Scheme 1. The chemical structure of phenazopyridine.

rutile phases has been reported. Zachariah et al. [20] demonstrated that the photocatalytic activity of mixed-phase TiO_2 nanoparticles was a function of rutile content with the maximum photocatalytic activity observed for 40 wt% rutile. Su et al. [28] also investigated the influence of the anatase-to-rutile ratios on their photoreactivities. A TiO_2 film with ~60 wt% anatase and ~40 wt% rutile exhibited optimal performance and a 50% improved activity compared with pure anatase. However, Pal et al. [29] observed that TiO_2 microspheres prepared by spray drying and calcined at 400 °C with 52.2 wt% of rutile phase achieved the best photocatalytic efficiency for degradation of dyes. It is clear that the TiO_2 phase contents and their ratios are the key factors in optimizing their photocatalytic activities. The optimum ratio between the different phases is the focus of these current studies.

Compared with TiO_2 nanopowders, one dimensional TiO_2 fibers have attracted considerable attention in recent years for photocatalytic applications [30,31] due to their higher surface-to-volume ratio [32], improved light absorption through the light scattering within the porous structure [32], and faster electron diffusion to the surface [33,34]. Here, we report TiO_2 polycrystalline sub-micron fibers prepared with different rutile fractions ranging from 0 wt% to 100 wt% by adjusting their calcination temperature. These fibers were applied to the photocatalytic degradation of a model pharmaceutical agent, phenazopyridine [2,6-diamino-3-(phenylazo)-pyridine hydrochloride, (PAP)] (Scheme 1), which is used commercially as an analgesic for urinary tract infections [35,36]. To our knowledge, this is the first study on optimization of photocatalytic performance of electrospun TiO_2 fibers with different rutile fractions. Physical characterization combined with the determination of initial degradation rate constant provides insights into the mechanism and optimization of these fibrous materials for decontaminating toxic pharmaceutical agents in aqueous waste streams and for application to industrial and environmental pollutants as well.

2. Experimental

2.1. Materials

Polymethylmethacrylate (PMMA) ($M_w = 960,000$ g/mol), titanium isopropoxide (TTIP), *N,N*-dimethylformamide anhydrous (DMF), chloroform, Degussa P25, and phenazopyridine hydrochloride (PAP) ($M_w = 249.70$ g/mol) were all purchased from Sigma-Aldrich and used as received.

2.2. Synthesis of TiO_2 polycrystalline sub-micron fibers

TiO_2 polycrystalline sub-micron fibers were prepared by a typical sol-gel synthesis followed by electrospinning of polymer sol-gel and calcination treatment of polymer fibers as shown in the schematic presented in Fig. 1. A polymeric sol-gel was generated by stirring and hydrolysis of TTIP using 1:2 mass ratio of PMMA:TTIP, where 320 mg of PMMA was completely dissolved in 2 mL of chloroform followed by drop wise addition of 640 mg of TTIP with continuous stirring for 30 min. 2 mL of DMF was then added and stirred for another 2 h to increase the dielectric constant of the composite solution to aid in the electrospinning process. The

kinematic and absolute viscosity of the sol-gel solution at room temperature were 60.72 cSt and 0.071 Ns/m², respectively.

As shown in Fig. 1, the electrospinning working distance was fixed at 11 cm. The syringe was tilted 4° below the horizontal level. The sol-gel solution can reach the syringe tip by its gravity with a flow rate of 0.5 mL/min. 25 kV was the optimal voltage for continuous formation of smooth polymer fibers. The high voltage pulled the precursor sol-gel from the syringe onto the conductive Al collector forming polymer fibers. The resulting polymer fibers were left overnight to allow for complete hydrolysis of TTIP to $\text{Ti}(\text{OH})_4$ and further condensation to amorphous TiO_2 [37] followed by calcination treatment to create TiO_2 crystal phases. Pre-calcined polymer fibers are composed of PMMA, amorphous TiO_2 and residual solvent remaining following the electrospinning process. By adjusting the calcination temperatures from 285 to 600 °C for 4 h, TiO_2 fibers with varying content fractions of anatase and rutile phases can be fabricated under ambient atmosphere.

2.3. Photodegradation procedure

PAP solution with concentration of 144 μM was prepared using distilled water as a solvent. After blanking the UV-vis spectrophotometer with distilled water in a quartz cell, an initial reading (marked as $t = -60$ min) was taken by diluting 0.5 mL of PAP solution with 3.0 mL of distilled water. 12 mL of PAP solution was transferred into a 16 mL cylindrical quartz container and placed in the dark. Next, 12 mg of TiO_2 fibers were added into the 12 mL of PAP solution with constant stirring. After 30 and 60 min stirring in the dark, a 1.0 mL aliquot of the sample was taken and centrifuged for 5 min, which were recoded as sample of $t = -30$ min and $t = 0$ min separately. Once the sample at $t = 0$ min was taken, a UV lamp was turned on at a fixed distance of 9 cm from the center of the quartz cell and a 1.0 mL aliquot of the sample was taken at certain intervals (10, 20, 30, 45, 60 min) and centrifuged for 5 min. Once the centrifuging was complete, 0.5 mL of the upper solution was taken and diluted with 3.0 mL of distilled water. The diluted sample was run through the UV-vis spectrophotometer and an absorbance spectrum was obtained as $t = -30, 0, 10, 20, 30, 45, 60$ min.

2.4. Characterization methods

The pre-calcined polymer fibers were fabricated using a high voltage Spellman SL 30 generator, where a high electrical potential was applied across the syringe needle attached to a copper wire and the collector screen. The photodegradation experiments were performed using an Oriel 66001 UV lamp with Oriel 68805 40–200 W universal Arc lamp power supply, which covered all the UV range with wavelength from 100 to 400 nm. The lamp power supplied 12 A, 120 V and 240 W. The distance between the center of the solution container and the UV lamp was controlled at 9 cm. UV-vis analysis of the aliquot was performed on an 8452A Hewlett Packard Diode Array spectrophotometer instrument with the wavelength from 190 to 820 nm to characterize the absorption spectrum of each aliquot to determine the PAP concentration. Sample analyses for photodegradation were performed in distilled water unless otherwise noted. The morphological and structural characteristics of the pre-calcined polymer fibers and post-calcined TiO_2 fibers were measured using the field emission scanning electron microscope (FESEM, Supra 55 VP from Zeiss equipped with an EDAX energy dispersive X-ray spectroscopy detector), and X-ray diffraction (XRD, PANalytical's X'Pert PRO Materials Research Diffractometer with $\text{Cu K}\alpha$ X-radiation ($\lambda = 1.5418$ Å)), respectively. TEM images were obtained from JEOL 2010 FETEM instrument. The TEM samples were dispersed in EtOH by sonication and the resulting solution were placed on a lacey carbon grid, which was left in air to evaporate the solvent. Thermogravimetric analysis (TGA)

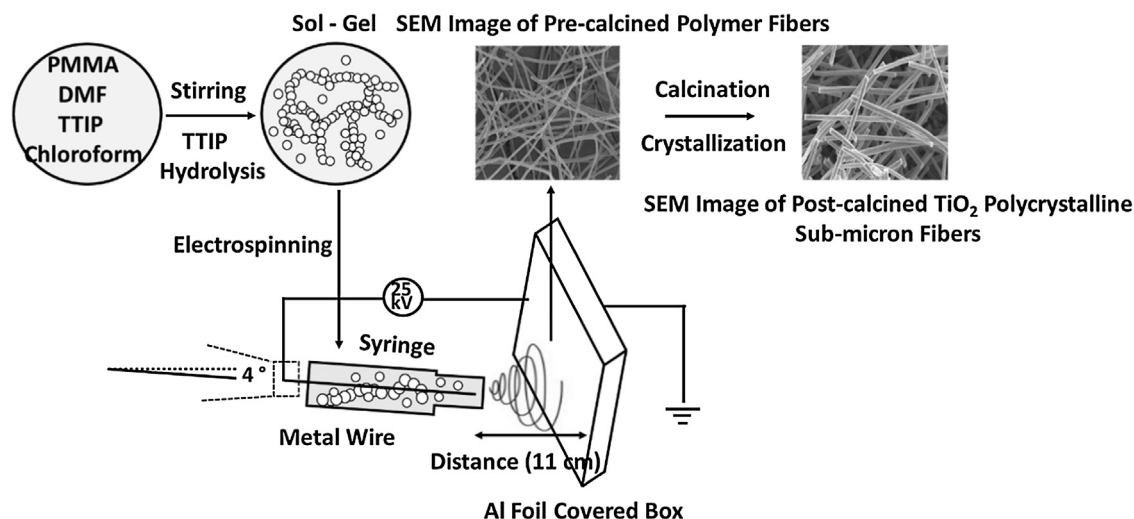


Fig. 1. Schematic figure showing the processes involved in the fabrication of TiO_2 polycrystalline sub-micron fibers including sol-gel preparation, electrospinning using polymer sol-gel solution and calcination treatment of polymer fibers.

was done using Netzsch TG 209 F1 Iris with QMS 403 Aeolus. Differential scanning calorimetry (DSC) measurements were done using TA instruments Q200 with a finned air cooling system. The conditions were $20^\circ\text{C}/\text{min}$ ramp rates from room temperature to 800°C using air as the gas. Raman analyses were performed using Thermo Scientific DXR Raman microscope with the laser wavelength of 532 nm . The Raman peaks were reported over the range from 50 to 3400 cm^{-1} . The kinematic and absolute viscosity of the sol-gel solution were measured at room temperature using a Cannon-Fenske Viscometer. Optical absorption spectra were recorded using JASCO V-650 UV-vis spectrophotometer with the ILV-724 integrating sphere accessory. Data was taken from 200 to 800 nm with a data interval of 1 nm and a scan rate of $200\text{ nm}/\text{min}$. The PL spectra were recorded using a Lumex Ltd. Fluorat-02 spectrometer with excitation wavelength of 300 and 350 nm . Nitrogen adsorption isotherms were measured for post-calcined TiO_2 fibers using a Micromeritics 3Flex Surface Characterization Analyzer at 77 K . Prior to analysis, each material was activated overnight at 100°C under a flow of dry nitrogen. Brunauer–Emmett–Teller (BET) modeling was performed to obtain the specific surface areas.

3. Results and discussion

3.1. Characterization of TiO_2 polycrystalline sub-micron fibers

Pre-calcined polymer fibers and post-calcined TiO_2 polycrystalline sub-micron fibers after calcination at 285 , 320 , 360 , 400 and 600°C for 4 h under ambient atmosphere were investigated using scanning electron microscope. As shown in Fig. 2, each type of fiber had a uniform diameter and dispersed without evidence of aggregation. The diameter of the fibers decreased from 848.9 ± 74.0 to $457.7 \pm 46.2\text{ nm}$ as the calcination temperature increased to 600°C as shown in Table 1. This decrease in diameter was related to the polymer matrix decomposition and phase transformation because the anatase-to-rutile phase transformation was known to be accompanied by approximately a 10% decrease in the volume [18]. Magnified SEM images of the fibers were shown as inserts and demonstrated that the pre-calcined polymer fibers had a wrinkled surface morphology and TiO_2 fibers after calcination at 285 , 320 , 360 and 400°C all maintained that wrinkled surface morphology as indicated by the arrows. When the calcination temperature increased to 600°C , the morphology of the fibers showed a much smoother surface. Compared with the pre-calcined polymer fibers,

the crystal grains inside the post-calcined TiO_2 fibers started to form. The grains became larger as the calcination temperature increased and they were measured based on the inserted cross section SEM images and listed in Table 1 as G_{SEM} .

To better understand the surface morphology and grain size changes, pre-calcined polymer fibers and post-calcined TiO_2 polycrystalline sub-micron fibers after calcination at 285 , 320 , 360 , 400 and 600°C for 4 h under ambient atmosphere were also investigated using transmission electron microscope. In Fig. 3a, it showed a porous structure in the pre-calcined polymer fibers. Post-calcined TiO_2 fibers were made of TiO_2 grains with different sizes after calcination under different temperatures. Growth between grains and grain aggregations are also observed in Fig. 3b–f. When the calcination temperature increased from 285 to 600°C , the grain size increased dramatically from approximate 15 nm to more than 50 nm , which was consistent with the grain size measured from SEM images.

The XRD patterns of pre-calcined polymer fibers and post-calcined TiO_2 polycrystalline sub-micron fibers at 285 , 320 , 360 , 400 and 600°C with 4 h holding times under ambient atmosphere are shown in Fig. 4. The XRD pattern of the pre-calcined polymer fibers showed a largely amorphous phase. As the calcination temperature was increased, well defined diffraction peaks for the post-calcined TiO_2 fibers appeared, which suggested the presence of both anatase and rutile phases. Pure anatase and rutile fibers could be observed after calcination at 285 and 600°C , respectively. For the anatase phase, the major peaks were obtained at 2θ values of 25.5 , 37.9 , 48.2 , 53.8 , and 55.0° representing the Miller indices of (101) , (004) , (200) , (105) , and (211) planes, respectively. For the rutile phase, peaks were observed at 2θ values of 27.6 , 36.1 , 41.2 , and 54.3° , respectively, representing the Miller indices of (110) , (101) , (111) , and (211) planes, respectively. The weight fraction of rutile phase in the post-calcined TiO_2 fibers can be calculated from the equation of $W_R = 1/[1 + 0.8(I_A/I_R)]$ [20,28], where I_A is the X-ray integrated intensities of the (101) reflection of anatase at 2θ of 25.5° and I_R is that of the (110) reflection of rutile at 2θ of 27.6° . It was clearly seen that I_A/I_R decreased with increasing calcination temperature. The weight fraction of rutile phase in TiO_2 fibers was found to increase with increasing calcination temperature from 0% to 100% shown in Table 1. According to the Scherrer Equation [18–20,29], the grain sizes of anatase phase and rutile phase were calculated based on $A(101)$ and $R(110)$ in the XRD pattern and listed in Table 1 as G_{XRD} . G_{XRD} showed a consistent trend

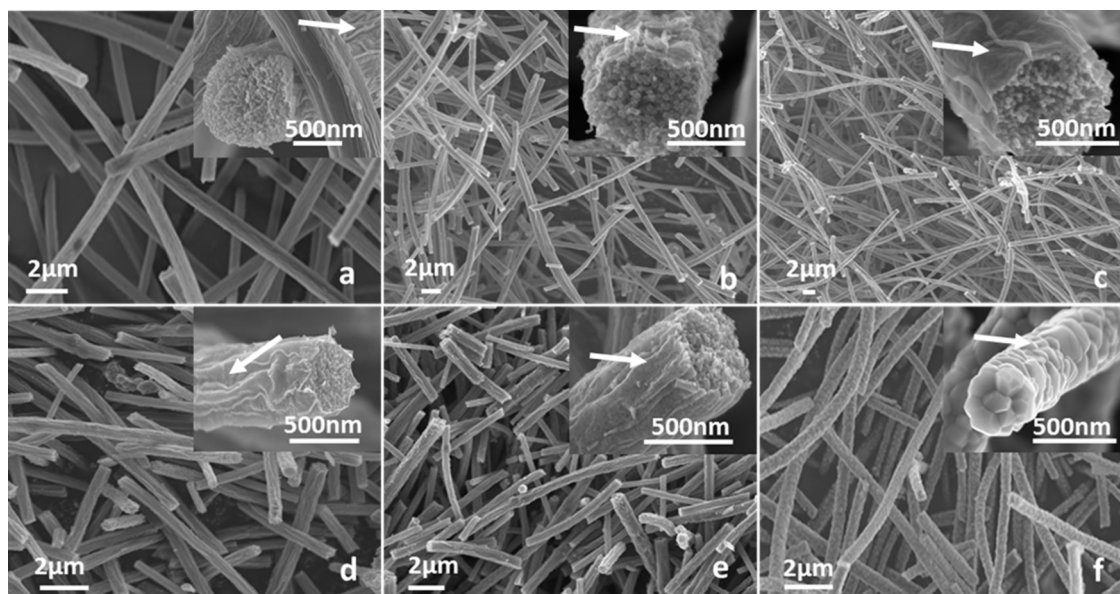


Fig. 2. SEM images of (a) pre-calcined polymer fibers; post-calcined TiO₂ polycrystalline sub-micron fibers after (b) 285, (c) 320, (d) 360, (e) 400, (f) 600 °C calcination for 4 h under ambient atmosphere. Inserted cross section SEM images were used to measure their grain sizes and the arrows pointed at their surface showing their surface morphologies.

Table 1

Pre-calcined polymer fibers and post-calcined TiO₂ polycrystalline sub-micron fibers prepared under different temperature calcination conditions showing different diameters, rutile fractions and grain sizes. The grain sizes calculated and measured from XRD patterns and SEM images were marked as G_{XRD} and G_{SEM} , respectively.

Sample in SEM image	Calcination temperature (°C)	Fiber diameter(nm)	Rutile fraction(%)	Anatase G_{XRD} (nm)	Rutile G_{XRD} (nm)	G_{SEM} (nm)
a	N/A	849 ± 74	N/A	N/A	N/A	N/A
b	285	723 ± 75	0	7	N/A	21 ± 2
c	320	668 ± 71	16	11	16	24 ± 2
d	360	570 ± 58	38	13	23	25 ± 3
e	400	487 ± 47	67	17	25	28 ± 4
f	600	458 ± 46	100	N/A	34	67 ± 5

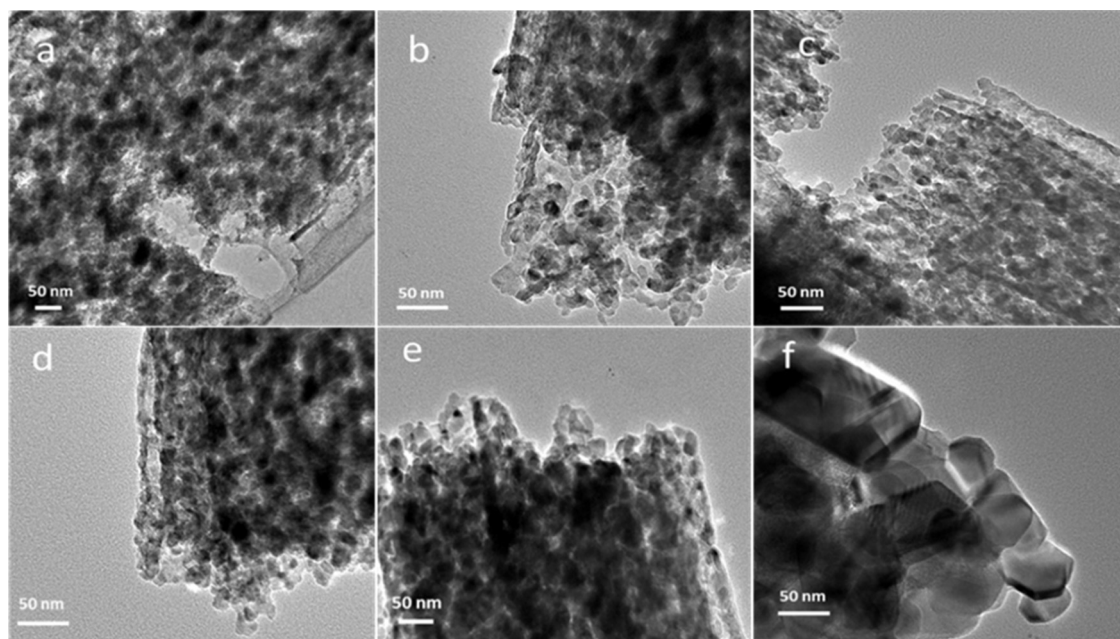


Fig. 3. TEM images of (a) pre-calcined polymer fibers; post-calcined TiO₂ polycrystalline sub-micron fibers after (b) 285, (c) 320, (d) 360, (e) 400, (f) 600 °C calcination for 4 h under ambient atmosphere.

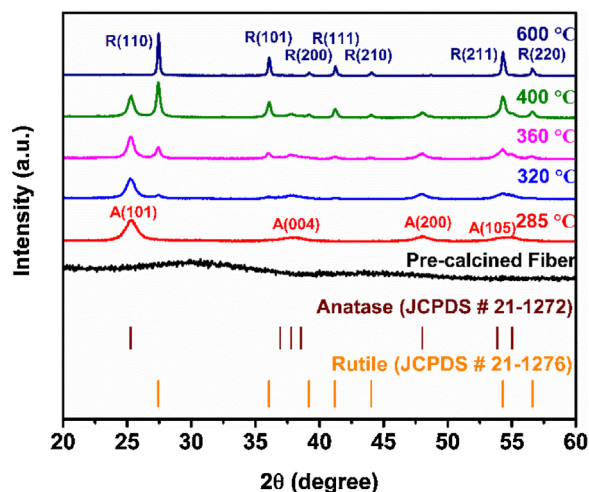


Fig. 4. XRD patterns of pre-calcined polymer fibers and post-calcined TiO_2 polycrystalline sub-micron fibers after 285, 320, 360, 400 and 600 °C calcination for 4 h under ambient atmosphere, where the “A” and “R” in the figure denote the anatase and rutile phase of TiO_2 , respectively.

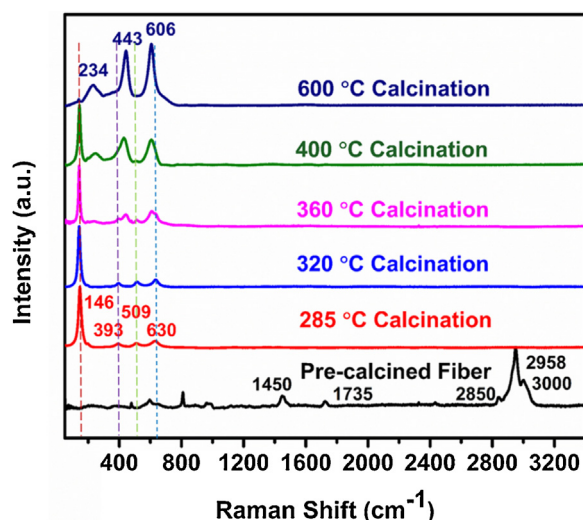


Fig. 5. Raman spectra of pre-calcined polymer fibers and post-calcined TiO_2 sub-micron fibers after 285, 320, 360, 400 and 600 °C calcination for 4 h under ambient atmosphere.

with G_{SEM} that the size of anatase and rutile grains both increased as the rutile fraction increased. This suggested that the transformation from anatase to rutile phase and the grains growth happened simultaneously. G_{SEM} was larger than G_{XRD} , which was considered to be the aggregation of grains inside the fibers. Baiju et al. [18] explained this size differences calculated using XRD and SEM as a result of TiO_2 powder aggregation having different average aggregation size, average nanoparticle size, and average nanocrystallite size.

In order to confirm that PMMA existed in the pre-calcined polymer fibers and it completely decomposed in the post-calcined TiO_2 fibers, Raman analysis was performed on pre-calcined polymer fibers and post-calcined TiO_2 fibers. As shown in Fig. 5, Raman peaks can be detected at 1450, 1735, 2850, 2958, 3000 cm^{-1} for pre-calcined polymer fibers, which confirmed the presence of PMMA. For the post-calcined TiO_2 fibers under different calcination temperatures, the PMMA peaks completely disappeared, which suggested PMMA decomposed during the calcination process. Anatase phase showed characteristic peaks in Raman spectra at 146, 393, 509 and 630 cm^{-1} and rutile phase showed peaks at

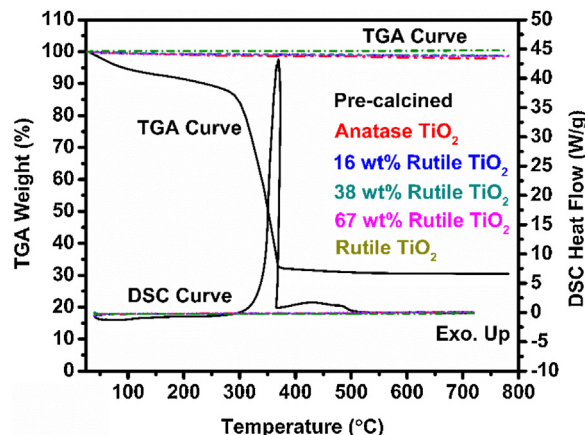


Fig. 6. TGA and DSC curves of pre-calcined polymer fibers and post-calcined TiO_2 sub-micron fibers with rutile fraction of 0 wt%, 16 wt%, 38 wt%, 67 wt% and 100 wt%.

234, 443 and 606 cm^{-1} . As the calcination temperature increased from 285 to 600 °C, Raman peaks of the anatase phase disappeared leaving only rutile phase peaks. This Raman result is consistent with the information from XRD patterns.

As shown in Fig. 6, TGA and DSC measurement were performed on the pre-calcined polymer fibers and post-calcined TiO_2 fibers with different rutile fractions. For pre-calcined polymer fibers, TGA curves showed that 13% weight loss was observed before 285 °C from the adsorbed solvent and surface water on the fibers. PMMA started to decompose around 285 °C and the decomposition continued until 370 °C. It contained approximate 56% of PMMA in the pre-calcined polymer fibers. Between 370 and 800 °C, no further weight loss was observed and 31% of the sample was left. It was considered as TiO_2 with amorphous phase coming from TTIP hydrolysis. In the DSC curve, there was a sharp exothermic peak at about 350 °C, which was mainly due to the decomposition of PMMA. Between 400 and 500 °C, another exothermic peak appeared, which was attributed to the phase transition from amorphous TiO_2 to TiO_2 polycrystalline. For TiO_2 fibers with different rutile fractions, TGA and DSC curves overlapped together. No weight loss and heat flow happened between room temperature and 700 °C, which indicated there were no PMMA left in post-calcined TiO_2 fibers. It further confirmed the fact that PMMA polymer matrix decomposed during the calcination process.

3.2. Photocatalytic activity and mechanism

In order to study the influence of the rutile weight fraction in TiO_2 sub-micron fibers on the photodegradation activities, six degradation experiments were performed under identical condition as shown in Fig. 7. The 144 μM PAP solution was used as the initial pollutant for the photodegradation experiments. Based on the UV–vis absorbance peak changes at 428 nm, the PAP concentration changes were observed both in the dark and under UV irradiation and plotted as a function of time. Pure PAP solution without any catalyst present was very stable under both dark and UV irradiation conditions. As the weight fraction of the rutile phase increased up to 38 wt%, the photodegradation activity of the TiO_2 fibers was found to improve. However, further increase of the rutile fraction led to slower degradation activity. All of the PAP solution was completely degraded within 45 min by using the TiO_2 sub-micron fibers with 38 wt% of rutile phase. Degussa-P25 was also used for comparison on the photocatalytic performance. As it showed in Fig. 7, in the first 30 min under UV irradiation, P25 has a better degradation performance than 38 wt% rutile fibers. However, after 30 min irradiation the degradation rate of P25 got slower.

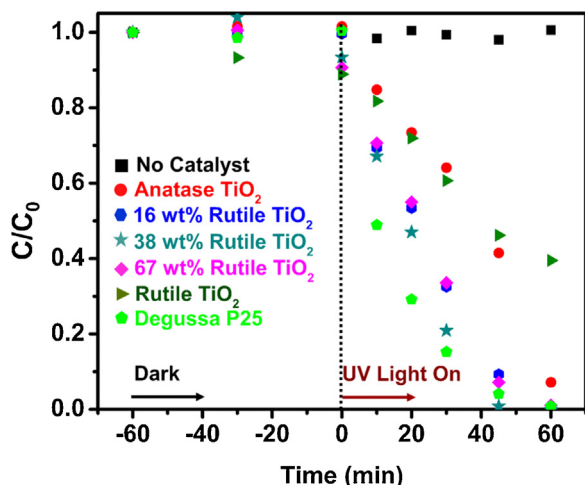


Fig. 7. PAP concentration changes based on liquid UV-vis spectroscopy on aliquots picked up at $t = -60, -30, 0, 10, 20, 30, 45, 60$ min using TiO_2 sub-micron fibers with different rutile fractions.

At $t = 45$ min, the performance of 38 wt% rutile fibers surpassed the degradation performance of P25.

The degradation data from Fig. 7 could be best fit as a pseudo-first-order reaction. The rate constant and the kinetic equation can be expressed as $C = C_0 e^{-kt}$, where t is the reaction time; k is the rate constant; C_0 and C are the PAP initial concentration and concentration at reaction time of t , respectively. The initial degradation rate constant k during the first 30 min degradation period using five TiO_2 fibers with different rutile fractions were calculated. They were plotted with the rutile fractions as a function of calcination temperature shown in Fig. 8a. It is clear that the initial degradation rate constant of TiO_2 polycrystalline sub-micron fibers strongly depended on the rutile fraction in the mixed-phase fibers, which could be tuned through the calcination temperature. The optimal initial rate constant was 0.044 min^{-1} using TiO_2 fibers with 38 wt% of rutile after calcination at 360°C for 4 h under ambient atmosphere.

In order to determine the possible reasons that TiO_2 polycrystalline sub-micron fibers with 38 wt% of rutile phase exhibited the optimal initial PAP photodegradation rate constant, specific surface area of the five TiO_2 fibers was measured by Brunauer-Emmett-Teller (BET) method and plotted with their initial rate constants as a function of their rutile fractions in Fig. 8b. The results demonstrate that as the rutile fraction increased, the surface area of the TiO_2 fibers decreased. This suggested that the TiO_2 fibers with higher fraction of rutile phase had a lower surface area. This surface area result was consistent with the surface morphology observation from SEM images in Fig. 2. If other factors were not considered, higher surface area would leave more active sites to interact with H_2O , O_2 , and PAP to generate more active radicals and to achieve a faster initial rate constant for the degradation of PAP. In this way, one could hypothesize that TiO_2 fibers with higher surface area would adsorb more PAP in the dark and have a better initial rate constant under UV irradiation. However, as shown in Fig. 8c, TiO_2 fibers with higher surface area had a lower adsorption of PAP in the dark, which indicated that the surface properties of the fibers would affect the PAP adsorption-desorption process in the dark. In addition, the TiO_2 fibers with 38 wt% of rutile and surface area of $39 \text{ m}^2/\text{g}$ had the best initial rate constant of 0.044 min^{-1} rather than pure anatase fibers with the higher surface area of $50 \text{ m}^2/\text{g}$. This result supports that the surface area is not the only factor in affecting the photodegradation activity. There should be one or more other factors playing a role in the photodegradation process and overall photocatalytic activity.

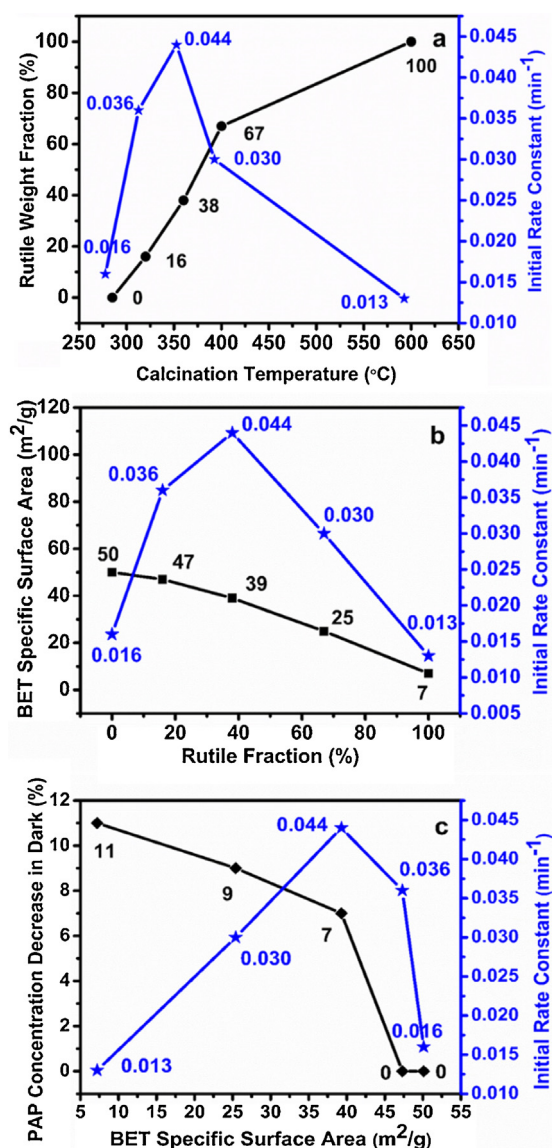


Fig. 8. Rutile weigh fraction, specific surface area and first 30-min initial degradation rate constants for photodegradations using post-calcined TiO_2 polycrystalline sub-micron fibers with different rutile fractions after calcination at 285, 320, 360, 400, 600°C for 4 h under ambient atmosphere.

The grain size difference between different post-calcined TiO_2 polycrystalline sub-micron fibers was regarded to be another possible factor that could influence the initial degradation rate constant. According to the anatase G_{XRD} and rutile G_{XRD} in Table 1 calculated from Scherrer equation, the grain size was plotted as a function of rutile fraction shown in Fig. 9a. Both the anatase and rutile grain sizes increased with increasing rutile fraction. The TiO_2 sub-micron fibers with medium grain size (anatase G_{XRD} of 13 nm, rutile G_{XRD} of 23 nm and G_{SEM} of 25 ± 3 nm) were found to have the optimal initial degradation rate constant shown in Fig. 9b. This could be explained by the existence of an optimal grain size for TiO_2 photocatalytic efficiency.

There are two types of e^-/h^+ recombination, which occur either inside the bulk (volume recombination) or on the surface (surface recombination). Volume recombination will be a dominant process within large grains. However, when the grain size decreases to smaller sizes, the surface recombination on the grains will weaken the charge carrier transfer process between the grains because surface recombination is much faster than that of the interfacial charge

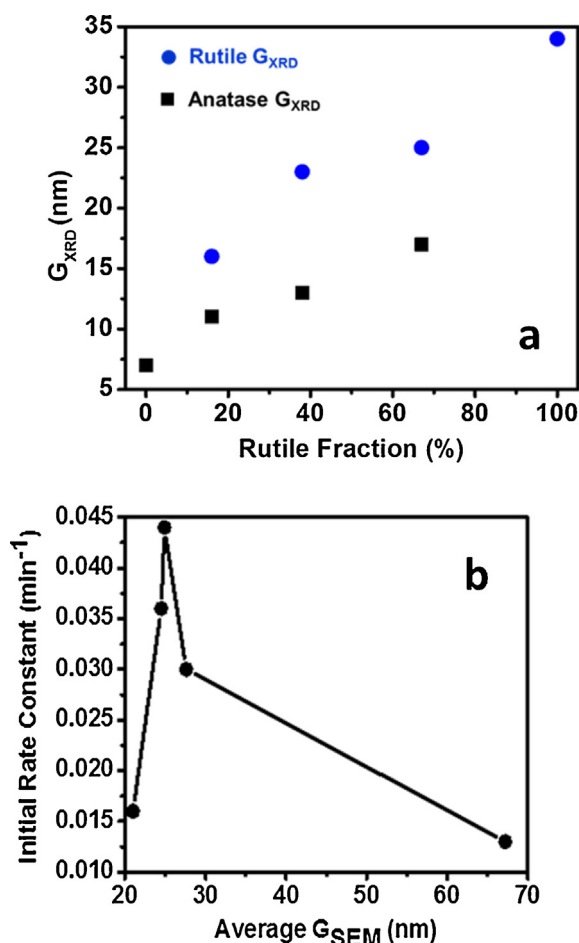


Fig. 9. Anatase and rutile grain size in post-calcined TiO_2 polycrystalline sub-micron fibers with different rutile fractions and the relationship between average grain size and their related initial degradation rate constant.

transfer. Therefore, an optimal electron transfer grain size would be expected to exist. This argument about the optimal grain size is supported by Zhang et al. [19] who reported that TiO_2 particles with a diameter of 13.3 nm had the longest emission decay time. For post-calcined TiO_2 sub-micron fibers with the same diameter, larger grain sizes would make the e^-/h^+ hop to the fiber surface faster and should lead to increased reaction rates. In Fig. 2, SEM images demonstrated that post-calcined TiO_2 sub-micron fibers

with higher rutile fractions had a smaller diameter and a larger grain size. It suggests that 100% rutile fibers should have the fastest charge diffusion rate during the degradation process. However, 100% rutile fibers with the largest grain size would also have the largest e^-/h^+ volume recombination, which limits the yield of e^-/h^+ diffusing to the surface despite the faster diffusion rate.

Besides the influence of surface area and grain size, the rutile fraction was another possible factor leading to the different initial rate constants. Recently a new understanding of the band alignment between rutile and anatase TiO_2 showed that the electron affinity of anatase was higher than rutile [38]. This suggests that it is thermodynamically favorable for electron transfer from rutile to anatase. This would help explain the enhanced electron–hole separation during the photodegradation process of PAP. The hypothesized electron transfer diagram is shown in Fig. 10 showing the favorable migration of photoexcited electrons from the conduction band of rutile to conduction band of anatase. At the same time, the electrons in the valence band of rutile are also favorable to migrate into the valence band of anatase. This electron transfer process could also be regarded as the holes transport from anatase to rutile. This flow of electrons will effectively increase the effective charge separation and consequently improve the photocatalytic efficiency of the post-calcined TiO_2 sub-micron fibers.

Surface adsorbed H_2O and O_2 react with the electrons and holes trapped on the surface to form reactive hydroxyl radicals and superoxide radical anions, respectively as is also shown in Fig. 10. Both of the radicals are oxidants, among which the hydroxyl radical is an extremely powerful and indiscriminate oxidant. Hydroxyl radical can rapidly attack pollutants at the surface or in the solution [39]. These oxidizing radicals react with PAP leading to the cleavage of azo linkage and the decomposition into some smaller molecules [40]. The products of these redox reactions lead to regeneration of the ground state in the fibers for reuse in the photocatalysis.

The rutile fraction in TiO_2 fibers affected the optical band gap of the fibers. The band gap energy of TiO_2 fibers with different rutile fractions was determined from optical absorption spectrum recorded by a UV spectrophotometer compatible for solid sample analysis. $(\alpha h\nu)^2$ was used as Y axis to plot for the indirect band gap transitions from TiO_2 [41,42]. As shown in Fig. 11, the band gap energy of TiO_2 fibers was determined to be 3.16 eV, 3.12 eV, 3.06 eV, 3.03 eV and 3.02 eV with increasing rutile weight fraction, respectively. The inset plot shows that the band gap energy of TiO_2 nanofibers decreases as the rutile fraction increases. This shift can be elucidated as a consequence of the changes of fibers' diameter, grain size and surface energy [43].

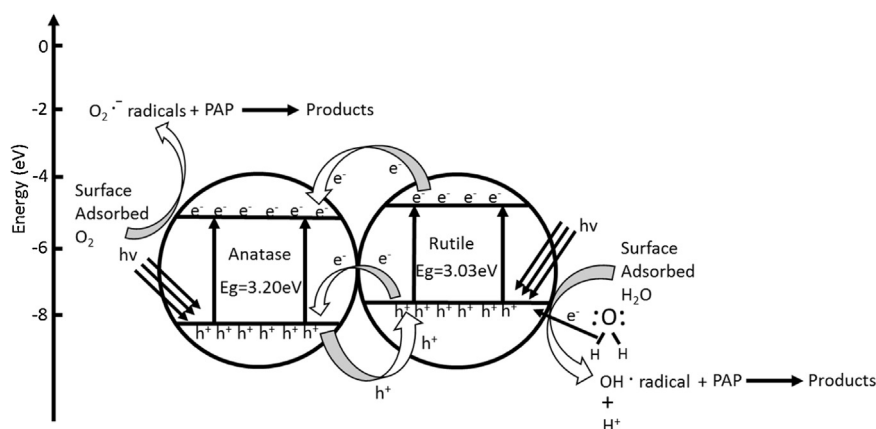


Fig. 10. Proposed schematic representation of possible electron–hole separation pathway mechanism for anatase and rutile mixed-phase TiO_2 sub-micron fibers during the photodegradation process of PAP.

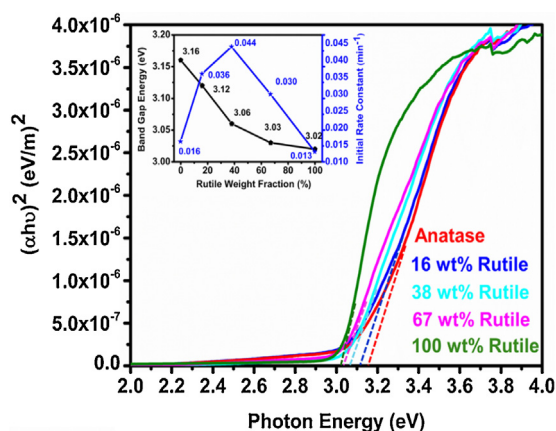


Fig. 11. Plot of $(\alpha h\nu)^2$ versus photon energy for calculating band gap energy of TiO_2 fibers with different rutile fractions. The inset shows that the band gap energy decreases with increase of rutile weight fraction in fibers.

The results shown above confirm our hypothesis that there are many possible factors involved in optimizing the photocatalytic performance of TiO_2 sub-micron fibers. As the calcination temperature increased, more of the anatase phase was transformed to rutile phase and the crystal grains became larger in the post-calcined TiO_2 fibers. This change made the surface area of post-calcined TiO_2 fibers decrease. Theoretically, the initial rate constant would decrease as a result of decreased specific surface area. However, more rutile phase in the post-calcined TiO_2 fibers help improve the electron–hole pair separation to increase the initial rate constant. In addition, the existence of an optimal grain size in post-calcined TiO_2 fibers balances the e^-/h^+ volume recombination, surface recombination, and charge diffusion rate. It is concluded that the combination of surface area, grain size and phase composition result in TiO_2 sub-micron fibers with 38 wt% of rutile phase having the optimal initial degradation rate constant.

4. Conclusion

TiO_2 polycrystalline sub-micron fibers with varying rutile fractions ranging from 0 wt% to 100 wt% were successfully synthesized from sol–gel solution followed by electrospinning and calcination at different temperatures under ambient atmosphere. As the calcination temperature increased, the rutile fraction in TiO_2 fibers increased and the surface area decreased. The photocatalytic activity showed that post-calcined TiO_2 fiber calcined at 360°C containing 38 wt% of rutile had the highest initial degradation rate constant and the fastest degradation efficiency for the degradation of PAP. A $144\ \mu\text{M}$ aqueous PAP solution could be completely degraded within 45 min. The existence of an optimum rutile fraction in TiO_2 sub-micron fibers can be explained by the combined influence between surface area, grain size and phase composition. TiO_2 fibers with the optimized rutile to anatase ratio provides a new type of material for future application in the pharmaceutical waste treatment and other environmental remediation.

Acknowledgements

We acknowledge funding from the National Science Foundation under grant number IIP-1318202, Strategic Partnership for Industrial Resurgence (SPIR) and the Army Research Office (ARO)W911NF1310235. Additional funding was provided by the Joint Science and Technology Office for Chemical Biological Defense (JSTO-CBD) under contract BA13PHM210 at the Edgewood Chemical Biological Center by Leidos, Inc. contract number

W911SR-10-D-0004-0014. This experimental work has been carried out with support from the Department of Chemistry at Binghamton University, State University of New York. The authors would like to further acknowledge Shirmonda Smith (Leidos, Inc.) for assistance with BET analysis conducted at the Edgewood Chemical Biological Center.

Appendix A. Supplementary data

Supplementary data associated with this article can be found, in the online version, at <http://dx.doi.org/10.1016/j.apcatb.2015.12.040>.

References

- [1] F. Abdulla, H.A. Qdais, A. Rabi, *Waste Manage.* 28 (2008) 450–458.
- [2] Q. Frederic, P. Yves, *Chemosphere* 115 (2014) 31–39.
- [3] H.S. Hilal, G.Y. Al-Nour, A. Zyoud, M.H. Helal, I. Saadeddin, *Solid State Sci.* 12 (2010) 578–586.
- [4] L.A. Pérez-Estrada, M.I. Maldonado, W. Gernjak, A. Agüera, A.R. Fernández-Alba, M.M. Ballesteros, S. Malato, *Catal. Today* 101 (2005) 219–226.
- [5] A.L. Borene, W.A. Arnold, K. McNeill, *Aquat. Sci.* 65 (2003) 320–341.
- [6] A. Chatzidakis, C. Berberidou, I. Paspaltsis, G. Kyriakou, I. Sklaviadis, I. Poullos, *Water Res.* 42 (2008) 386–394.
- [7] S. Kaniou, K. Pitarakis, I. Barlagianni, I. Poullos, *Chemosphere* 60 (2005) 372–380.
- [8] S. Ledakowicz, M. Solecka, R. Zylla, *J. Biotechnol.* 89 (2001) 175–184.
- [9] A. Fujishima, *Nature* 238 (1972) 37–38.
- [10] K. Dai, H. Chen, T. Peng, D. Ke, H. Yi, *Chemosphere* 69 (2007) 1361–1367.
- [11] J.M. Herrmann, C. Duchamp, M. Karkmaz, B.T. Hoai, H. Lachheb, E. Puzenat, C. Guillard, *J. Hazard. Mater.* 146 (2007) 624–629.
- [12] O. Carp, C.L. Huisman, A. Reller, *Prog. Solid State Chem.* 32 (2004) 33–177.
- [13] E. Bizani, K. Fytianos, I. Poullos, V. Tsiridis, *J. Hazard. Mater.* 136 (2006) 85–94.
- [14] H.S. Hilal, L.Z. Majjad, N. Zaatar, A. El-Hamouz, *Solid State Sci.* 9 (2007) 9–15.
- [15] C. Chen, Z. Wang, S. Ruan, B. Zou, M. Zhao, F. Wu, *Dyes Pigments* 77 (2008) 204–209.
- [16] Y. Li, X. Li, J. Li, J. Yin, *Water Res.* 40 (2006) 1119–1126.
- [17] R.J. Tayade, P.K. Surolia, R.G. Kulkarni, R.V. Jasra, *Sci. Technol. Adv. Mater.* 8 (2007) 455–462.
- [18] K.V. Baiju, S. Shukla, K.S. Sandhya, J. James, K.G.K. Warriar, *J. Phys. Chem. C* 111 (2007) 7612–7622.
- [19] Z. Zhang, C.C. Wang, R. Zakaria, J.Y. Ying, *J. Phys. Chem. B* 102 (1998) 10871–10878.
- [20] A. Zachariah, K.V. Baiju, S. Shukla, K.S. Deepa, J. James, K.G.K. Warriar, *J. Phys. Chem. C* 112 (2008) 11345–11356.
- [21] Z. Ding, G.Q. Lu, P.F. Greenfield, *J. Phys. Chem. B* 104 (2000) 4815–4820.
- [22] U. Stafford, K.A. Gray, P.V. Kamat, A. Varma, *Chem. Phys. Lett.* 205 (1993) 55–61.
- [23] D.C. Hurum, A.G. Agrios, K.A. Gray, T. Rajh, M.C. Thurnauer, *J. Phys. Chem. B* 107 (2003) 4545–4549.
- [24] G. Riegel, J.R. Bolton, *J. Phys. Chem.* 99 (1995) 4215–4224.
- [25] K. Nagaveni, G. Sivalingam, M.S. Hegde, G. Madras, *Appl. Catal. B* 48 (2004) 83–93.
- [26] M. Kolar, J. Mešt'ánková, J. Jirkovský, M. Heyrovský, J. Šubrt, *Langmuir* 22 (2006) 598–604.
- [27] G. Tian, H. Fu, L. Jing, B. Xin, K. Pan, *J. Phys. Chem. C* 112 (2008) 3083–3089.
- [28] R. Su, R. Bechstein, L. Sø, R.T. Vang, M. Sillassen, B. Esbjörnsson, A. Palmqvist, F. Besenbacher, *J. Phys. Chem. C* 115 (2011) 24287–24292.
- [29] S. Pal, A.M. Laera, A. Licciulli, M. Catalano, A. Taurino, *Ind. Eng. Chem. Res.* 53 (2014) 7931–7938.
- [30] E.A. Obuya, W. Harrigan, D.M. Andala, J. Lippens, T.C. Keane, W.E. Jones, *Mol. Catal. A Chem.* 340 (2011) 89–98.
- [31] E.A. Obuya, P.C. Joshi, T.A. Gray, T.C. Keane, W.E. Jones, *Int. J. Chem.* 6 (2014) 1–16.
- [32] M. Lu, C. Shao, K. Wang, N. Lu, X. Zhang, P. Zhang, M. Zhang, X. Li, Y. Liu, *ACS Appl. Mater. Interfaces* 6 (2014) 9004–9012.
- [33] X. Zhang, V. Thavasi, S.G. Mhaisalkar, S. Ramakrishna, *Nanoscale* 4 (2014) 1707–1716.
- [34] Y.I. Lee, J.S. Lee, E.S. Park, D.H. Jang, J.E. Lee, K. Kim, N.V. Myung, Y.H. Choa, *J. Nanosci. Nanotechnol.* 14 (2014) 8005–8009.
- [35] M. Citak, S. Yilmaz, Y. Dilgin, G. Turker, S. Yagmur, H. Erdugan, N. Erdugan, *Curr. Pharm. Anal.* 3 (2007) 141–145.
- [36] S. Yagmur, S. Yilmaz, M. Sadikoglu, G. Saglikoglu, M. Yildiz, C. Yengin, E. Kilinc, *Int. J. Electrochem. Sci.* 8 (2013) 6818–6828.

- [37] S. Mahshid, M. Askari, M.S. Ghamsari, *J. Mater. Process. Technol.* 189 (2007) 296–300.
- [38] D.O. Scanlon, C.W. Dunnill, J. Buckeridge, S.A. Shevlin, A.J. Logsdail, S.M. Woodley, C.R.A. Catlow, M.J. Powell, R.G. Palgrave, I.P. Parkin, G.W. Watson, T.W. Keal, P. Sherwood, A. Walsh, A.A. Sokol, *Nat. Mater.* 12 (2013) 798–801.
- [39] S. Sun, J. Ding, J. Bao, C. Gao, Z. Qi, C. Li, *Catal. Lett.* 137 (2010) 239–246.
- [40] M. Fathinia, A. Khataee, *Appl. Catal. A. Gen.* 491 (2015) 136–154.
- [41] R. Lopez, R. Gomez, *J. Sol–Gel Sci. Technol.* 61 (2012) 1–7.
- [42] S. Ebraheem, A. El-Saied, *Mater. Sci. Appl.* 4 (2013) 324–329.
- [43] K. Mondal, S. Bhattacharyya, A. Sharma, *Ind. Eng. Chem. Res.* 53 (2014) 18900–18909.